Multi-topology-Mode Grid-Connected Inverter to Improve Comprehensive Performance of Renewable Energy Source Generation System

Fengjiang Wu, *Member, IEEE*, Xiaoguang Li, Fan Feng, and Hoay Beng Gooi, *Senior Member, IEEE*

***Abstract*—The multi-inverter-based configuration is usually adopted in the renewable energy source grid-connected generation system (RES-GGS) to obtain a wide operational range and independent output power control of the renewable energy sources (RESs). The complicated configuration inevitably reduces the European efficiency. This paper proposes a multi-topology-mode inverter suitable for RES-GGS, which possesses five equivalent topology modes. When the output voltage and power of the RESs increase gradually, the system transforms its actual topology mode from the complicated ones to the simpler ones to increase the European efficiency. Furthermore, a system-level control strategy that can achieve the independent generation power control of each RES and the grid current closed-loop control is proposed. By online transforming the system among the five topology modes, the characteristics of wide operational range, independent output power control of each RES and high European efficiency are all achieved. The detailed experimental results verify the feasibility and advantages of the proposed multi-topology-mode grid-connected inverter.**

***Index Terms*—Improvement of comprehensive performance, independent power control, multi-topology-mode grid-connected inverter, renewable energy source (RES) generation.**

I. INTRODUCTION

DUE to the challenge of the energy shortage and environmental pollution and because of its advantages of consuming no fossil fuels, infinite reserves, and harmlessness for the environment, the renewable energy source grid-connected generation system (RES-GGS) has attracted more and more attention [1]–[3]. At present, the initial investment cost of the RES-GGS is still high and the competitive edge of the RES-GGS is reduced. Therefore, how to enhance the power extraction ability and increase the utilization rate of the RES is a key issue in the RES-GGS. The solution is helpful to shorten the payback period and the competition of the RES-GGS will be enhanced significantly.

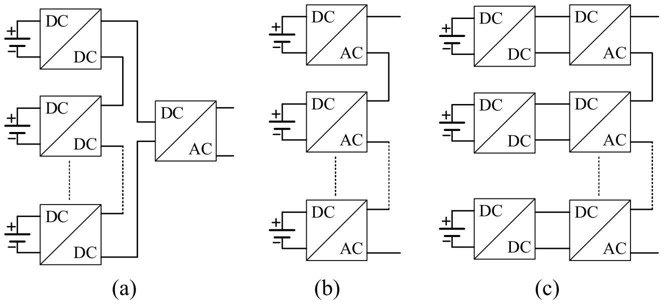

Fig. 1. Three kinds of distributed power electronics solutions for RES-GGS with independent power control ability. (a) DC optimizer; (b) single-stage cascaded multilevel inverter; and (c) two-stage cascaded multilevel inverter.

When the output voltages and power of the typical RESs vary in a wide range, in order to transmit continuously the generation power of the RESs to the grid, the power electronics based grid-connected inverter (GCI) are usually integrated with RESs to form an RES-GGS [4]–[6]. The routes of increasing the utilization rate of the RESs based on the RES-GGSs mainly include the following three aspects:

1) A wide operational range is required for the GCI to increase the power extraction from the RESs. Two requirements should be satisfied if the operational range of the system is widened. The first one is to keep the equivalent dc-bus voltage of the GCI larger than the amplitude of the grid voltage in the entire operational range, and the second one is that the total harmonics distortion (THD) of the grid current should meet the specific grid-connected standard in the entire operational range [7], [8].
2) Considering that a large number of distributed RESs are usually integrated together in the RES-GGSs to increase the total output power, the GCI should have the ability of the independent output power control of each RES to enhance the generation power of the [9]–[11].
3) The improvement of the operational efficiency in the entire operational range, which is defined as European Efficiency or California Efficiency needs to be considered [12], [13].

Up to now, the following several classical topologies possessing the functions of the independent output power control of the RESs and wide operational range are usually used in the

---

Manuscript received September 1, 2015; revised June 5, 2016 and April 10, 2016; accepted July 1, 2016. Date of publication July 11, 2016; date of current version February 2, 2017. This work was supported by the Energy Innovation Programme Office (EIPO) through the National Research Foundation and by the Singapore Economic Development Board. Recommended for publication by Associate Editor V. Agarwal.

F. Wu is with the School of Electrical and Electronic Engineering, Nanyang Technological University, Singapore 639798, Singapore, and also with the Department of Electrical Engineering, Harbin Institute of Technology, Harbin 150001, China (e-mail: shimeng@hit.edu.cn).

X. Li is with the Department of Electrical Engineering, Harbin Institute of Technology, Harbin 150001, China (e-mail: lixiaoguanghit@163.com).

F. Feng and H. B. Gooi are with the School of Electrical and Electronic Engineering, Nanyang Technological University, Singapore 639798, Singapore (e-mail: FFENG003@e.ntu.edu.sg; ehbgooi@ntu.edu.sg).

Color versions of one or more of the figures in this paper are available online at http://ieeexplore.ieee.org.

Digital Object Identifier 10.1109/TPEL.2016.2589974

RES-GGS. The first one is shown in Fig. 1(a) and named as dc optimizer, in which each RES is connected with a specific dc–dc converter and the output of these converters are connected in series to increase the total dc-bus voltage [11]. The output power of each RES can be independently controlled by independently tuning the power of each dc–dc converter. The second one is the classical cascaded multilevel topology shown in Fig. 1(b) [14]. The output voltage of the multilevel inverter is a multilevel waveform and only a small filter inductance can make the grid current THD meet the grid-connected standard. Furthermore, the independent output power control of the RESs is achieved by independently tuning the amplitudes and phase angles of the output voltages of the each dc–ac inverter contained in the multilevel inverter. The last one is the two-stage cascaded multilevel inverter shown in Fig. 1(c) [15], [16]. On the one hand, the advantage of the multilevel inverter is retained, and on the other hand, the introduction of the dc–dc inverter widens the generation range of the RESs and achieve the independent output power control of the RESs.

Although the topologies mentioned above are complicated, the ability of the independent power control of each RES and wide operational range enhances the generation power extraction of the RESs and they have a high practical value in the field of RES-GGS. However, because all of the power switches in these topologies are always under operating state, the system losses are large and the operational efficiency will be reduced, especially the European efficiency. Therefore, it is very difficult to achieve simultaneously the functions of wide operational range, independent power control of each RES and high European efficiency in these topologies.

In this paper, considering the characteristics of the RESs that their output voltages and power increase with the increase of the wind, irradiance and ambient temperature, a multi-topology-mode GCI (MTM-GCI) with five equivalent topology modes is proposed to improve the comprehensive performance of RES-GGS. The loss models and grid current THD expressions of each topology mode are derived, and the optimal operational ranges of each topology mode are accordingly obtained. Furthermore, a system-level control strategy for the proposed MTM-GCI, which can realize the independent generation power control of each RES and grid current closed-loop control in each topology mode, is proposed. Taking the condition of the grid current THD meeting the specific grid-connected standard as the requirement, when the output voltages and power of the RESs increase gradually, the system transforms its topology mode from the complicated one to the simpler one to increase the operational efficiency. Thus, the system will possesses simultaneously the characteristics of the wide operational range, the independent power control of the RESs and the high European efficiency and relatively small ac-side filter inductance. Finally, the proposed topology is compared in detail with the two topologies shown in Fig. 1(a) and (c) to highlight the advantages of the proposed one.

II. PROPOSED MULTI-TOPOLOGY-MODE GCI

The structure of the proposed MTM-GCI is shown in Fig. 2. A boost type dc–dc converter is connected in series with an H-bridge dc–ac inverter (HBI) to constitute a basic conversion unit. Two basic conversion units are cascaded to form the standard two-stage cascaded multilevel inverter (TCMI). Introducing the dc–dc converter not only improves the dc-bus voltage to extend the operational range but also realizes the independent power control of each RES.

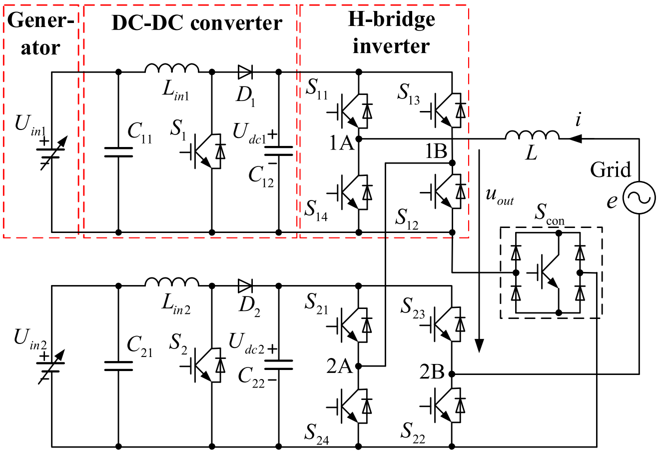

Fig. 2. Schematic of proposed multi-topology-mode GCI.

A bidirectional switch $S_{\rm con}$ is added into the TCMI to connect the negative terminals of the two basic conversion units. Then the connection of the two basic conversion units can be transformed between the cascaded mode and equivalent single HBI mode and accordingly, the proposed MTM-GCI is able to deduce five topology modes by adjusting the states of the power switches. When $S_{\rm con}$ is off, the inverter is a TCMI as shown in Fig. 3(a). The two dc–dc converters are under operating state to obtain the widest operational range of the system. Furthermore, when one of the dc–dc converters shuts down, the inverter becomes a hybrid cascaded multilevel inverter (HYCMI) as shown in Fig. 3(b). When both of the dc–dc converters shut down, the inverter becomes a cascaded multilevel inverter (CMI) as shown in Fig. 3(c).

When S_{12} and S_{24} are turned off, while S_{13}, S_{21}, and $S_{\rm con}$ are turned on, the positive terminals of the two dc buses are connected together through S_{13} and S_{21}, and the negative terminals are connected together through $S_{\rm con}$. The connection relationship of the two base conversion units is transformed from series to parallel and S_{11}, S_{14}, S_{23}, and S_{22} make up an H-bridge inverter. After that when both of the dc–dc converters work, the inverter becomes a two-stage H-bridge inverter (THBI) and the simplified version is shown in Fig. 3(d). In theory, the operational range of THBI mode is very wide. However, limited by the actual boost voltage ratio of the dc–dc converter, the operational range of the THBI mode is smaller than that of TCMI mode. When one of the dc–dc converters shuts down, the inverter becomes a hybrid H-bridge inverter (HYHBI) and the simplified version shown in Fig. 3(e). Compared with the above three CMI-type topology modes, the number of the power switches under switching state of the two HBI-type topology modes is significantly reduced and the switching loss of the inverter will be reduced accordingly.

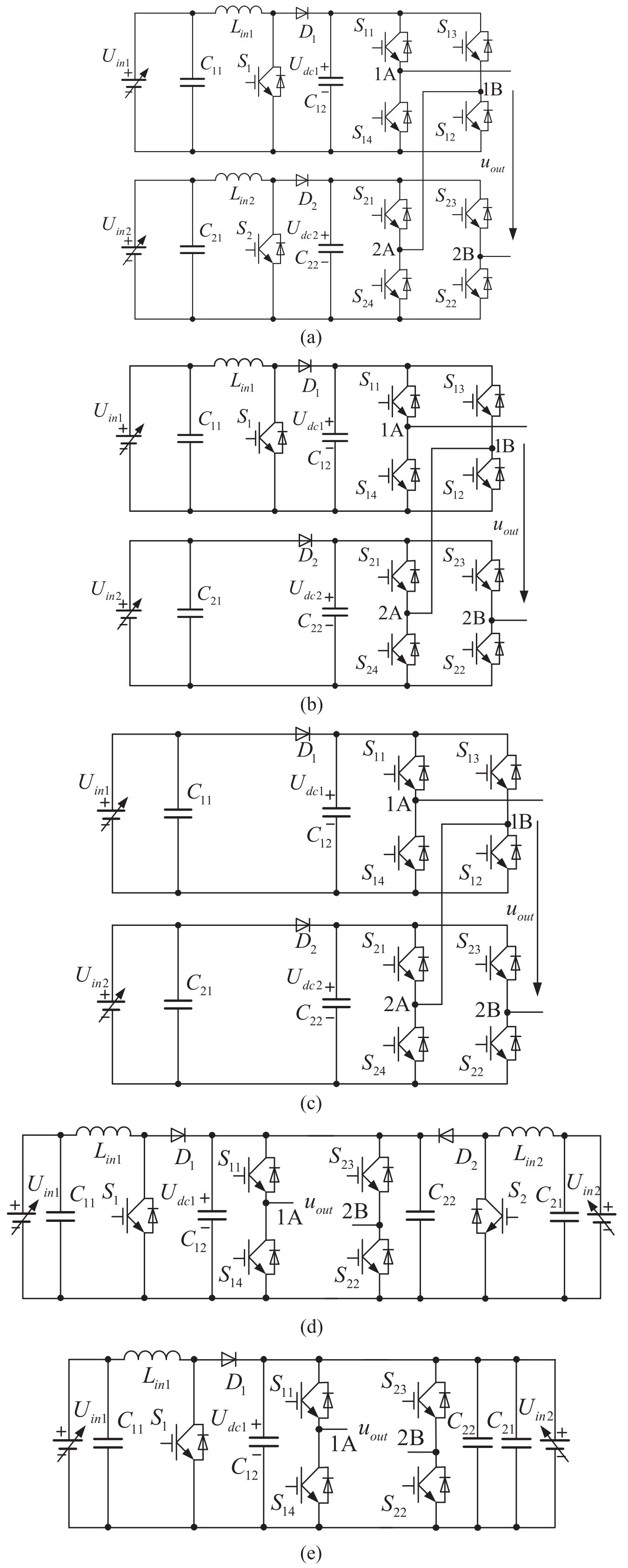

(a)

(b)

(c)

(d)

(e)

Fig. 3. Various equivalent topology modes of proposed MTM-GCI. (a) TCMI, (b) HYCMI, (c) CMI, (d) THBI, and (e) HYHBI.

III. DERIVATION OF POWER LOSSES, CURRENT THDS, AND OPERATIONAL RANGES OF FIVE TOPOLOGY MODES

It can be roughly inferred from the description above that because there are some difference between the structures of the five topology modes, the operational ranges, efficiency, and power quality of them will be different as well. So when the output voltage and power of the RESs vary in a wide range, by arranging a proper sequence of the five topology modes, the advantages of these topology modes will be fully utilized. Then the excellent comprehensive performance of the system in the entire operational range, including a wide operational range, independent power control of each RES and high European efficiency, can be simultaneously achieved. The expressions of the losses and grid current THDs of the five topology modes are derived later. Then the optimal operational range of each topology mode can be determined according to the theoretical analysis results.

A. Loss Models of the Five Topology Modes

Since each topology mode can be regarded as the combination of the dc–dc converters with the CMI or HBI, the linearized loss models of the dc–dc converters, CMI and HBI are respectively derived first. Then the loss models of each topology mode can be obtained according to the actual number of contained dc–dc converter and CMI or HBI. Because the ac filter inductor is a common component in all of the topology modes and to simplify the analysis, the loss of the ac filter inductor is not modeled.

The conduction and switching losses of the power switches and the loss of the dc inductor of the dc–dc converter are considered first. The instantaneous conduction losses of the IGBTs and diodes can be expressed linearly as [17]

$$P_{\text{con\_IGBT}} = U_{\text{ceI}} i_{\text{flow}} = (U_{\text{ceoI}} + R_{\text{onI}} i_{\text{flow}})\, i_{\text{flow}} \tag{1}$$

$$P_{\text{con\_diode}} = U_F i_{\text{flow}} = (U_{\text{FOD}} + R_{\text{onD}} i_{\text{flow}})\, i_{\text{flow}} \tag{2}$$

where U_{ceoI} and $R_{\text{onI}}, U_{\text{FOD}}$ and R_{onD} are the conduction saturation voltage drop and conduction-state resistance of IGBT and diode, respectively. i_{flow} is the current flowing through the power switch.

Neglecting the inductor current ripple, the conduction loss of the power switches of the dc–dc converter during one switching period can be expressed as

$$P_{\text{con\_dc}} = (U_{\text{ceoI}} + R_{\text{onI}} I_{\text{in}}) I_{\text{in}} d + (U_{\text{FOD}} + R_{\text{onD}} I_{\text{in}}) I_{\text{in}} (1 - d) \tag{3}$$

where I_{in} is the dc average current flowing through the power switch, d and T_{sdc} are the switch duty ratio and switching period of the dc–dc converter, respectively.

The switching loss of the dc–dc converter is analyzed as follows. It can be known from the principle of the boost converter that during any switching cycle, one IGBT is turned off and one IGBT is turned on, while one diode is turned off. The average switching loss of the dc–dc converter during one switching cycle can be obtained by dividing the switching loss energy during one switching cycle by the switching period and expressed as

$$P_{\text{sw\_dc}} = \frac{E_{ts1}}{T_{\text{sdc}}} \frac{I_{\text{in}}}{I_{\text{co}}} \frac{U_{\text{in}}}{U_{\text{ceo}}} \tag{4}$$

where E_{ts1} is the rated total switching loss energy of IGBT and diode. U_{ceo} and I_{co} are the rated turn-off voltage across the IGBT and the rated current flowing through the IGBT, respectively. U_{in} is the dc input voltage of the dc–dc converter. E_{ts1} can be read from the loss curves provided by the datasheet of the actual IGBT with specific I_{co} and U_{ceo}.

The dc filter inductor loss is derived as follows. The filter inductor loss is composed of the copper loss and the high-frequency iron loss. The copper loss can be expressed as

$$P_{\text{cop\_L}} = R_L I_{\text{in}}^2 \tag{5}$$

where R_L is the copper resistor of the dc filter inductor.

It is indicated by [18] that the high-frequency iron loss of the inductor is directly related to the high-frequency magnetic flux ripple peak ΔB. To simplify the analysis, the specific loss of the core material is expressed as a quadratic function of the root-mean-square (rms) value of ΔB. Furthermore, the high-frequency iron loss during one switching cycle can be calculated by multiplying the specific loss of the inductor by the volume of the filter inductor and expressed as

$$\begin{aligned} P_{h\_\text{L}} &= \frac{\text{Vol}_L}{T_{\text{sdc}}}\left(a\Delta B_{\text{rms}}^2 + b\Delta B_{\text{rms}} + c\right) \\ &= \frac{\text{Vol}_L}{T_{\text{sdc}}}\left[a\left(\frac{T_{\text{sdc}}U_{\text{in}}d}{2\sqrt{3}NA_e}\right)^2 + b\frac{T_{\text{sdc}}U_{\text{in}}d}{2\sqrt{3}NA_e} + c\right] \end{aligned} \tag{6}$$

where Vol_L, N and A_e is the volume, the number of the turns of the inductor coil and the iron sectional area of the inductor core, respectively. *a*, *b*, and *c* are the fitting parameters and determined by the actual specific loss curve of the core material. ΔB_{rms} is the rms value of ΔB.

In the following, the losses of the CMI and HBI are analyzed. A reusable modulation strategy suitable for the CMI and HBI is introduced and shown in Fig. 4 [19]. For CMI, the conventional CPS-SPWM is used [20]. Four carrier waves $T_{r1} - T_{r4}$ and modulation wave u_r are set to obtain the control signals of the power switches. In order to reduce the occupation of the controller resource, the control signals of the HBI are obtained by comparing u_r with T_{r1} and T_{r2}.

To save the page space, the detailed modeling process of the conduction loss of CMI is not shown here. The final total average conduction losses of IGBTs and diodes of CMI during one fundamental cycle are expressed as

$$\begin{aligned} \bar{p}_{\text{con\_CMI}} = {} & \left(\frac{4}{\pi} + M\right) U_{\text{ceoI}} I_m + \left(1 + \frac{8M}{3\pi}\right) R_{\text{onI}} I_m^2 \\ & + \left(\frac{4}{\pi} - M\right) U_{\text{FOD}} I_m + \left(1 - \frac{8M}{3\pi}\right) R_{\text{onD}} I_m^2 \end{aligned} \tag{7}$$

where E_m and ω are the amplitude and frequency of the grid voltage, respectively. I_m is the amplitude of the grid current. $M = \sqrt{E_m^2 + (\omega L I_m)^2}/(2U_{dc})$ is the amplitude modulation ratio of CMI and L is the ac-side filter inductance. U_{dc} is the dc-bus voltage of the basic conversion unit.

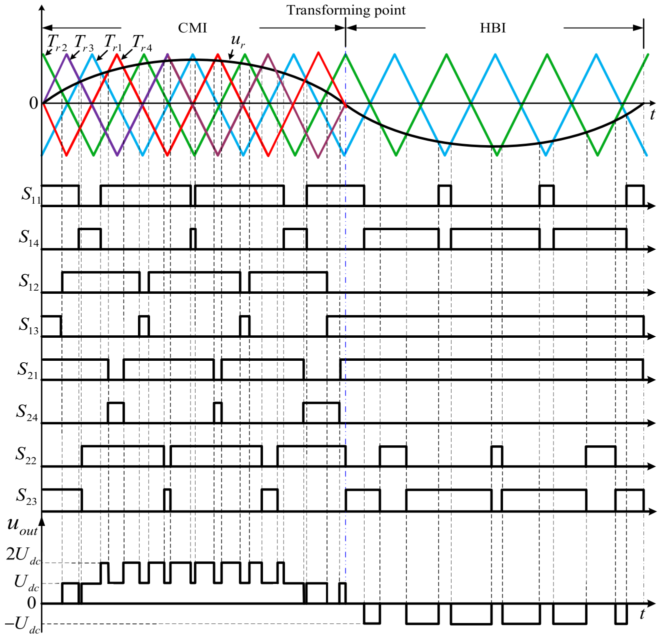

Fig. 4. Schematic of reusable SPWM strategy for the MTM-GCI.

As seen from Fig. 4, during any switching cycle, one IGBT and one diode are turned off and one IGBT and one diode is turned on. The total average switching loss of CMI during one fundamental cycle is calculated as

$$P_{\text{sw\_CMI}} = \frac{2}{\pi} f_s \int_0^{\frac{\pi}{2}} E_{ts}\, d(\omega t) = \frac{8}{\pi} f_c E_{ts1} \frac{I_m}{I_{\text{co}}} \frac{U_{\text{dc}}}{U_{\text{ceo}}} \tag{8}$$

where f_s is the switching frequency and f_c is the carrier frequency.

The average conduction losses of the power switches of HBI during one fundamental cycle are expressed as

$$\begin{aligned} \bar{p}_{\text{con\_HBI}} = {} & \left(\frac{4}{\pi} + \frac{M}{2}\right) V_{\text{ceoI}} I_m + \left(1 + \frac{2M}{3\pi}\right) R_{\text{onI}} I_m^2 \\ & + \left(\frac{5}{\pi} - \frac{7M}{4}\right) V_{\text{FOD}} I_m + \left(\frac{5}{4} - \frac{16M}{3\pi}\right) R_{\text{onD}} I_m^2 . \end{aligned} \tag{9}$$

The total average switching losses of HBI during one fundamental period can be calculated as

$$P_{\text{sw\_HBI}} = \frac{4}{\pi} f_c E_{\text{ts1}} \frac{I_m}{I_{\text{co}}} \frac{U_{\text{dc}}}{U_{\text{ceo}}}. \tag{10}$$

The total losses of various topology modes are finally obtained as follows according to the principle of these topology modes and the aforementioned loss expressions of the dc–dc converter, CMI, and HBI.

TCMI contains two dc–dc converters and CMI. Then the total loss of TCMI can be expressed as

$$\begin{aligned} P_{\text{TCMI}} = {} & 2\left(P_{\text{con\_dc}} + P_{\text{sw\_dc}} + P_{\text{cop\_L}} + P_{\text{h\_L}}\right) \\ & + \bar{p}_{\text{con\_CMI}} + P_{\text{sw\_CMI}}. \end{aligned} \tag{11}$$

HYCMI contains one dc–dc converter and CMI. Then the total loss of HYCMI can be expressed as

$$\begin{aligned} P_{\mathrm{HYCMI}} = \; & P_{\mathrm{con\_dc}} + P_{\mathrm{sw\_dc}} + P_{\mathrm{cop\_L}} + P_{h\_\mathrm{L}} \\ & + \bar{p}_{\mathrm{con\_CMI}} + P_{\mathrm{sw\_CMI}}. \end{aligned} \tag{12}$$

The total loss of CMI can be expressed as

$$P_{\mathrm{CMI}} = \bar{p}_{\mathrm{con\_CMI}} + P_{\mathrm{sw\_CMI}}. \tag{13}$$

THBI contains two dc–dc converters and HBI. Then the total loss of THBI can be expressed as

$$\begin{aligned} P_{\mathrm{THBI}} = \; & 2\left(P_{\mathrm{con\_dc}} + P_{\mathrm{sw\_dc}} + P_{\mathrm{cop\_L}} + P_{h\_\mathrm{L}}\right) \\ & + \bar{p}_{\mathrm{con\_HBI}} + P_{\mathrm{sw\_HBI}}. \end{aligned} \tag{14}$$

HYHBI contains one dc–dc converter and HBI. Then the total loss of HYHBI can be expressed as

$$\begin{aligned} P_{\mathrm{HYHBI}} = \; & P_{\mathrm{con\_dc}} + P_{\mathrm{sw\_dc}} + P_{\mathrm{cop\_L}} + P_{h\_\mathrm{L}} \\ & + \bar{p}_{\mathrm{con\_HBI}} + P_{\mathrm{sw\_HBI}}. \end{aligned} \tag{15}$$

B. Grid Current THDs

The relationship between the current THD and current ripples can be expressed as [7], [8]

$$\mathrm{THD} = \sqrt{I_2^2 + I_3^2 + I_4^2 + I_5^2 + \cdots}/I_1 \approx \Delta I_{\mathrm{rms}}/I_1 \tag{16}$$

where I_1 and I_i $(i = 2, 3, \ldots)$ are the rms value of the fundamental and each harmonic component of the grid current. ΔI_{rms} is the rms value of the actual grid current ripple.

For the CMI, when $M > 0.5$, the rms value of the current ripple during one fundamental period is calculated as

$$\Delta i_{\mathrm{rms1}} = \frac{1}{4f_c}\sqrt{\frac{1}{3\pi L^2}}\cdot \sqrt{\begin{aligned} & \sqrt{4M^2-1}\begin{pmatrix} -\frac{4}{3}E_m^2 - \frac{1}{24}\frac{E_m^2}{M^2} - \frac{8}{3}U_{\mathrm{dc}}E_m M \\ -\frac{1}{3M}U_{\mathrm{dc}}E_m - \frac{13}{2}U_{\mathrm{dc}}^2 \end{pmatrix} - \frac{16}{3}U_{\mathrm{dc}}E_m M^2 \\ & - \left(6U_{\mathrm{dc}}^2 M^2 + 8U_{\mathrm{dc}}E_m M + \frac{1}{2}E_m^2 + 4U_{\mathrm{dc}}^2\right)\arcsin\frac{1}{2M} \\ & + \pi\left(\frac{3}{4}E_m^2 M^2 + 4U_{\mathrm{dc}}^2 M^2 + 4U_{\mathrm{dc}}E_m M + \frac{1}{4}E_m^2 + 2U_{\mathrm{dc}}^2\right) \end{aligned}}. \tag{17}$$

When $M \leq 0.5$, the rms value of the current ripple during one fundamental period is

$$\Delta i_{\mathrm{rms2}} = \frac{1}{2f_c}\sqrt{\frac{M^2}{6\pi L^2}\left(\frac{3}{16}\pi E_m^2 + \frac{1}{4}\pi U_{\mathrm{dc}}^2 - \frac{4}{3}U_{\mathrm{dc}}E_m\right)}. \tag{18}$$

As for the HBI, the rms value of the current ripple during one fundamental cycle is calculated as

$$\Delta i_{\mathrm{rms\_HBI}} = \frac{1}{f_c}\sqrt{\frac{M^2}{6\pi L^2}\left(\frac{3}{16}\pi E_m^2 + \frac{\pi}{4}U_{\mathrm{dc}}^2 - \frac{4}{3}U_{\mathrm{dc}}E_m\right)}. \tag{19}$$

Then the current THDs of CMI and HBI can be obtained by substituting (17)–(19) into (16).

TABLE I
DATA OF PARAMETERS OF GCI, DC SUPPLY SOURCES, AND GRID

Parameter	Value	Parameter	Value
$U_{\mathrm{in1}}, U_{\mathrm{in2}}$	100–500 V	$I_{\mathrm{in1}}, I_{\mathrm{in2}}$	10 A
E_m	311 V	f_{sdc}	10 kHz
ω	314 rad/s	$L_{\mathrm{in\,1}}, L_{\mathrm{in\,2}}, L$	1.5 mH
$U_{\mathrm{dc1}}, U_{\mathrm{dc2}}$	500 V	f_c	5 kHz
U_{ceoI}	0.6 V	R_{onI}	0.005 Ω
U_{FOD}	0.7 V	R_{onD}	0.0044 Ω
VOL_L	3150 cm^3	E_{ts}	14.9 mJ
I_{co}	200 A	U_{ceo}	300 V
R_L	0.017 Ω	A_e	105 cm^2
N	50	a	0.00015
b	0.0000075	c	0.00000025

C. Comparison and Determination of Optimal Operational Ranges of Various Topology Modes

In this part, the losses and grid current THDs of the five topology modes are compared with each other in detail. Then when the output voltage and power of the RESs vary in a wide range, the respective operational ranges of the five topology modes can be determined according to the comparison results and the comprehensive performance of the entire system can be improved. According to the earlier analysis, the actual power switch and filter inductor are chosen and the corresponding parameters can be determined. The curves of the losses, operational efficiencies and grid current THDs of the five topology modes with respect to the variation of the output voltage and power of the RESs can be drawn according to the aforementioned expressions and the determined values of various parameters. As a comparison, the curves of the standard one-stage HBI are also drawn. The Infineon IGBT FF200R06KE3 is selected as the power switch of the inverter. Then the parameters (125°C) in the former loss expressions are determined according to the datasheet of the IGBT and listed in Table I. The parameters of the GCI and the grid are also listed in it.

To simplify the analysis, the output currents of the RESs keep constant. The grid current amplitude can be calculated according to the power balance of the dc side and ac side. For TCMI, CMI, THBI and HBI, the reference value of the dc-bus voltage is 500 V and the output voltages of the two RESs vary simultaneously from 100 to 500 V. For HYCMI and HYHBI, the characteristics of the RES connected to the dc–dc converter under the working state is consistent with the aforementioned situations, while the output voltage of the other RES keeps at a constant of 500 V.

The corresponding curves are shown in Fig. 5. It can be inferred that the operational ranges, losses, efficiencies and current THDs of the five topology modes are different from each other. For the loss, the order corresponding to the same dc suple sources voltage U_{in1} can be approximately described from large to small as

$$\mathrm{TCMI} > \mathrm{HYCMI} > \mathrm{CMI} > \mathrm{THBI} > \mathrm{HYHBI} > \mathrm{HBI}.$$

The order of the efficiency is on the contrary. As for the grid current THD, the order corresponding to a constant U_{in1} can be

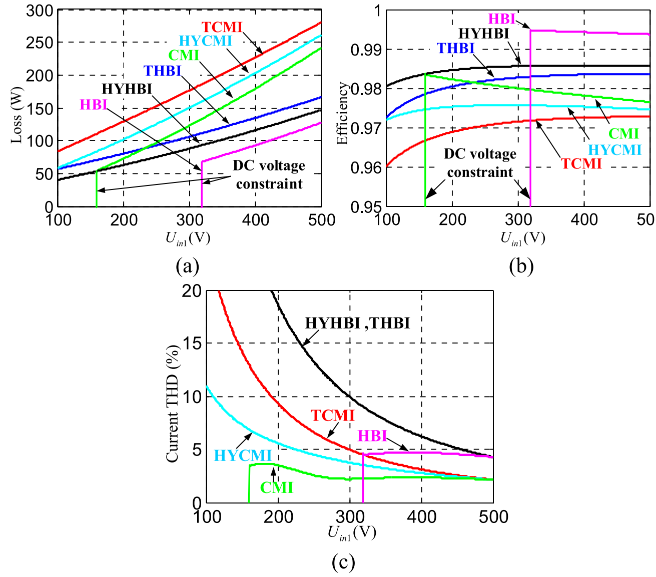

(a) (b)

(c)

Fig. 5. Distribution curves of various parameters of various topology modes. (a) Total loss. (b) Efficiency. (c) Current THD.

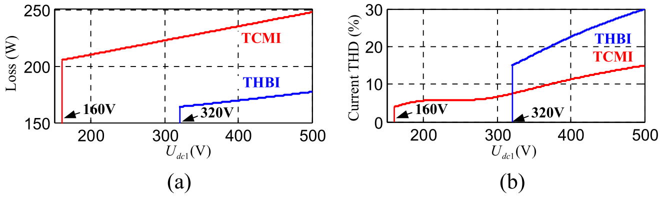

(a) (b)

Fig. 6. Distribution curves of TCMI and THBI corresponding to dc-bus voltage. (a) Total loss. (b) Current THD.

approximately described from large to small as

$$\text{THBI} = \text{HYHBI} > \text{HBI} > \text{TCMI} > \text{HYCMI} > \text{CMI}.$$

It can be known from the earlier analysis that within the entire operational range, each topology mode possesses its own superiority in terms of the operational range, grid current THD and operational efficiency relative to other topology modes. For example, the loss of HBI is the smallest, while the grid current THD is the biggest and the operational range is the narrowest. The loss of TCMI is the biggest, while its operational range is the widest. The grid current THDs of TCMI, HYCMI and CMI modes are generally smaller than those of THBI, HYHBI, and HBI modes. So when the output voltage and power of the two RESs vary in a wide range, the optimal comprehensive performance of the proposed MTM-GCI can be achieved by arranging a proper working sequence of the five topology modes according to the actual output voltage and power of the RESs.

The paper aims to achieve the excellent comprehensive performance of the GCI, such as the wide generation range of the RES, independent output power control of each RES, small ac-side filter inductance and high European efficiency. Meanwhile, the grid current THD is always smaller than the specific grid-connected standard in the entire operational range. The reason that the comprehensive performance of the GCI is improved by transforming the topology modes is illustrated later. It is well known that the output voltage and power of the RESs will vary in a wide range with the variation of the wind, irradiance and ambient temperature. It can be seen from Fig. 5(c) that when the output voltage and power of the RESs increase gradually, the grid current THDs of the five topology modes will decrease gradually as well. So when the output voltage and power of the RESs are small, the TCMI mode, which possesses the characteristics of the highest equivalent dc-bus voltage and the smallest grid current THD, is set as the actual topology of the system to achieve the widest operational range and reduce the ac-side filter inductance. When the output voltage and power of the RESs increase gradually, the equivalent dc-bus voltages of all of the topology modes will increase and the grid current THD of them will decrease. Then the topology mode of the system can be transformed into the simpler one and the constraint of the dc-bus voltage larger than the grid voltage amplitude (called grid-connected voltage requirement in this paper) is still satisfied and the European efficiency will be increased accordingly.

As the dc-bus voltage adopted in the earlier analysis has ensured that it is always larger than the grid voltage amplitude in the entire operational range, the function of TCMI and HYCMI cannot be fully embodied. Therefore, the loss and grid current THD curves of TCMI and THBI with respect to the dc-bus voltage with the constant output current and voltage of the RESs are drawn and shown in Fig. 6. It can be seen from Fig. 6 that both the losses and grid current THDs of the two topology modes increase as the dc-bus voltage increases. It means that the dc-bus voltage reference should be selected as low as possible to reduce the loss and grid current THD. The actual reference value of the dc-bus voltage can be easily determined by the following approach. The theoretical reference value of the dc-bus voltage is calculated first according to the voltage equation of the GCI and then the actual reference one can be obtained through multiplying a margin coefficient by the theoretical value.

According to the aforementioned analysis results, the selection rule of the optimal operational ranges of each topology mode is obtained to improve the comprehensive performance of the GCI. When the sum of the output voltage of these two RESs is smaller than the amplitude of the grid voltage and in order to extend the lowest level of the operational range, the inverter works at TCMI mode, in which both of the dc–dc converters are under working state. On the one hand, a larger boost dc voltage ratio can be realized by the dc–dc converter and the generation range of the RESs will be extent. On the other hand, when the output voltage and power of the RES is small, working in TCMI mode reduces the grid current THD so that only a small ac filter inductance is required to ensure the current THD meet the specific standard.

When the output voltage of any RES is larger than the reference value of the dc-bus voltage, which is set slightly larger than one half of the amplitude of the grid voltage, the corresponding dc–dc converter shuts down to reduce the loss and the inverter becomes HYCMI. When the output voltages of the two RESs are larger than the reference of the dc-bus voltage, both of the dc–dc converters shut down and the inverter becomes CMI. The loss of the system will be further reduced.

When the grid current THD of THBI meets the grid-connected standard, the inverter is transformed into THBI mode. On the one hand, the loss of the GCI can be reduced. On the other hand, the independent power control of these two RESs is still realized. In order to avoid the grid current spikes when transforming the CMI mode into the THBI mode, the transformation of the topology mode is done around the zero-crossing points of the reference modulation wave u_r. Since the GCI is usually controlled at a unity power factor, the phase angle difference between the output voltage of the inverter and the grid current is small. Thus the grid current is also small around the zero-crossing point of u_r. Furthermore, the control signals should be manually changed at the transformation point of the topology mode to ensure that the system is under freewheeling state during the topology transformation process.

After the system transforms into THBI mode, when the output voltage of any RES is larger than the reference value of the dc-bus voltage, the corresponding dc–dc converter shuts down to reduce the loss and the other dc–dc converter keeps working to ensure the independent power control of these two RESs. The system operates under HYHBI mode accordingly.

IV. SYSTEM-LEVEL CONTROL STRATEGIES OF FIVE TOPOLOGY MODES

The functions of the system-level control strategies mainly include the following: 1) ensuring that the dc-bus voltage meets the grid-connected voltage requirement; 2) maintaining independent power control of each RES; and 3) closed-loop controlling of the grid current.

In order to realize the aforementioned functions in each topology mode, the system-level control strategy is proposed in this paper and described as follows.

A. Control Strategies of Three CMI-Type Topology Modes

The ac side structures of the three topology modes are the same, so a common control strategy suitable for the three topology modes is designed and the schematic is shown in Fig. 7(a), where d_1 and d_2 are the duty ratios of the two dc–dc converters. To simplify the analysis, only the single closed-loop control structure of the output voltage of the dc–dc converter is used. The reference values of the output voltages of the two RESs are obtained by the maximum power point tracking (MPPT) strategy [14]. For the CMI, a double-modulation wave CPS-SPWM is adopted based on the strategy shown in Fig. 4. The phase angle of the two modulation waves u_{r1} and u_{r2} is identical while their amplitudes are different. The purpose is to realize the independent power control of the two RESs by regulating the amplitudes of the two modulation waves. The control signals of S_{11}, S_{14} and S_{12}, S_{13} are obtained by comparing u_{r1} with T_{r1} and T_{r2}, and the control signals of S_{22}, S_{23} and S_{21}, S_{24} are obtained by comparing u_{r2} with T_{r3} and T_{r4}.

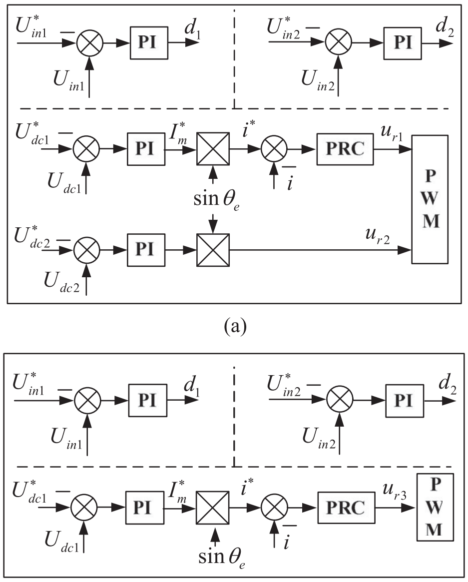

(a)

(b)

Fig. 7. Schematics of system-level control strategies of MTM-GCI. (a) Three CMI-type topology modes. (b) Two HBI-type topology modes.

For TCMI, both of the dc–dc converters are in working state to boost the two dc-bus voltages U_{dc1} and U_{dc2}. The single closed-loop control of the grid current based on a proportional–resonant controller (PRC) is used in the system to realize a zero steady-state error control of the grid current [21]. The output of the PRC is set as the first modulation wave u_{r1}. The other modulation wave u_{r2} is obtained by multiplying the sine value of grid voltage phase angle θ_e and the output of the closed-loop regulator of U_{dc2}. The respective control signals of each dc–ac inverter are obtained by inputting both of u_{r1} and u_{r2} into the CPS-SPWM algorithm.

It can be seen from the system-level control strategy shown in Fig. 7(a) that when the inverter is transformed from the TCMI into HYCMI, if assuming that the first dc–dc converter shuts down, only the control algorithm of the first dc–dc converter is not performed while the other part of the control algorithm is the same with the TCMI. Since the RES connected to the stopped dc–dc converter is equivalent to directly connect to the dc bus, the output voltage reference of the RES is set as the dc-bus voltage reference to implement the MPPT control of the RES, namely $U^*_{\mathrm{dc1}} = U^*_{\mathrm{in1}}$. When the system is transformed into CMI mode, the control algorithm of the two dc–dc converters do not work and other parts of the control algorithm are the same with the TCMI. To implement the MPPT control of the RESs, $U^*_{\mathrm{dc1}} = U^*_{\mathrm{in1}}$ and $U^*_{\mathrm{dc2}} = U^*_{\mathrm{in2}}$ are set. It can be known from the earlier analysis that the proposed system-level control strategy can automatically and smoothly switch between the three CMI-type topology modes.

B. Control Strategies of THBI and HYHBI

Because there is only one dc–ac inverter in the THBI and HYHBI modes, only one modulation wave is required. The control strategies of the two topology modes are shown in Fig. 7(b). For THBI, both of the dc–dc converters work under the closed-loop control of the RES output voltages to realize the independent power control of the two RESs. The control signals of various power switches are obtained by inputting the modulation

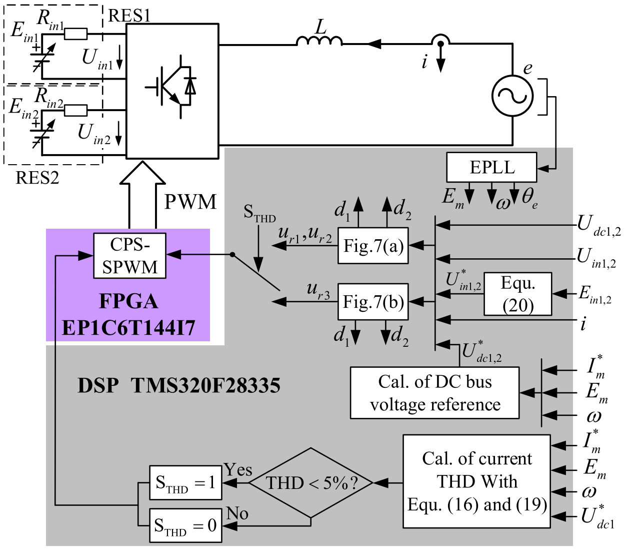

Fig. 8. Schematic of implementation platform of proposed MTM-GCI.

wave u_{r3} into the SPWM algorithm shown in Fig. 4. Utilizing the strategies above realizes not only the independent output power control of the RESs but also the stabilization of the dc-bus voltage. When the output voltage of either RES is larger than the dc-bus voltage reference, the corresponding dc–dc converter shuts down and the dc-bus voltage reference is set as the output voltage reference of the RES, while other control loops remain unchanged. In this case, the system has automatically switched into HYHBI mode. It can be known that the proposed control strategy suitable for the THBI and HYHBI modes realize the automatic and smooth transformation between the two topology modes.

V. EXPERIMENTAL VERIFICATION OF MTM-GCI

The lab experimental prototype of the MTM-GCI is set up and shown in Fig. 8. The experimental parameters are the same as the ones in Table I. The coefficients of the two PI controllers of the RES output voltages are set as $K_{\text{Puin}} = 0.02$ and $K_{\text{Iuin}} = 0.15$. The coefficients of the two PI controllers of the dc-bus voltages are also set the same and $K_{\text{Pudc}} = 0.1$ and $K_{\text{Iudc}} = 1.2$. The coefficients of the grid current PRC are set as $K_{\text{Pac}} = 0.5$ and $K_{\text{Rac}} = 7.5$. The amplitude, frequency and phase angle of the grid voltage are estimated by the single-phase enhanced phase-locked loop (EPLL) presented in [22].

When the system operates in THBI mode, it should ensure that the grid current THD $< 5\%$. The grid current THD is calculated from (16) and (19). When the grid current THD is less than 5%, $S_{\text{THD}} = 1$ is set and the signal is transported to FPGA. In this case, the system is transformed into THBI mode. The reference values of the dc-bus voltage of the three CMI-type topology modes and two HBI-type topology modes can be, respectively, calculated according to the voltage equations of the GCI.

In order to simulate the characteristics of the RESs with the finite output power, two adjustable dc supply sources are set and their output voltages meet the relationship of $E_{\text{in1}} = \sqrt{3}E_{\text{in2}}$. The output terminals of the two dc sources are connected with the resistors of $R_{\text{in1}} = R_{\text{in2}} = 1\,\Omega$. The relationship of the output voltage references of the two RESs and the output voltages of the dc sources are

$$U^*_{\text{in1}} = E_{\text{in1}} - 10 \quad U^*_{\text{in2}} = E_{\text{in2}} - 10. \tag{20}$$

The experiments results of the RES output voltages changing from 50 to 400 V are obtained. The initial reference values of the dc-bus voltages are set as $U^*_{\text{dc1}} = U^*_{\text{dc2}} = 170\text{ V}$ to meet the grid-connected voltage requirement. When $U_{\text{in1}} \leq 170\text{ V}$, the system works under TCMI mode. When $U_{\text{in1}} > 170\text{ V}$, the corresponding dc–dc converter shuts down and the system works in HYCMI mode. When $U_{\text{in2}} > 170\text{ V}$, another dc–dc converter also shuts down and the system works in CMI mode. It can be calculated from (19) that when $U_{\text{in1}} > 350\text{ V}$ the grid current THD of THBI will meet the grid-connected standard. Therefore, the system is transformed into THBI and $U^*_{\text{dc1}} = 380\text{ V}$ is set. When $U_{\text{in1}} > 380\text{ V}$, the corresponding dc–dc converter shuts down and the system becomes HYHBI mode. The performance of these five topology modes and the transformation process between them can be verified through the aforementioned working process.

The experimental results of the entire operational process of the system, including the experimental waveforms of various topology modes and the corresponding tested total losses and the grid current THDs, are all shown in Fig. 9. It can be seen from Fig. 9 that when U_{in1} is large than 50 V, the system starts and works in TCMI mode. The system transforms its topology modes between those five topology modes smoothly with the increase of the output voltages of the RESs. The output voltage waveforms of the three CMI-type topology modes are five levels and the spectral distributions of the grid currents are concentrated at four times of the carrier frequency and its integer multiple zones. For the THBI and HYHBI modes, the output voltage waveforms are three levels and the spectral distributions of the grid currents are concentrated at twice the carrier frequency and its integer multiple zones. It is consistent with the foregoing analysis.

During transforming CMI mode to THBI mode, almost no grid current overshoot occurs. It is because that the transformation of the topology mode is performed around the zero-crossing point of the modulation wave and the inverter is under freewheeling state. In addition, transforming CMI mode to THBI mode is equivalent that the connection of the two dc–ac inverters are transformed from series to parallel. It means that the equivalent total dc-bus voltage is reduced and the grid current amplitude accordingly reduces for a short time. Under the action of the grid current closed-loop controller, after about two fundamental periods of the dynamic process, the actual grid current tracks the reference one. The online transformation of the dc–ac topology modes is performed smoothly.

In addition, as the output power of the RESs are periodically fluctuant, it is difficult to accurately calculate the average power of the RESs by directly observing the output power waveforms. Therefore, the instantaneous output power waveforms are not given. According to the pre-set experimental conditions, the output power of the RES is proportional to its output voltage. The experimental results indicate that throughout the entire

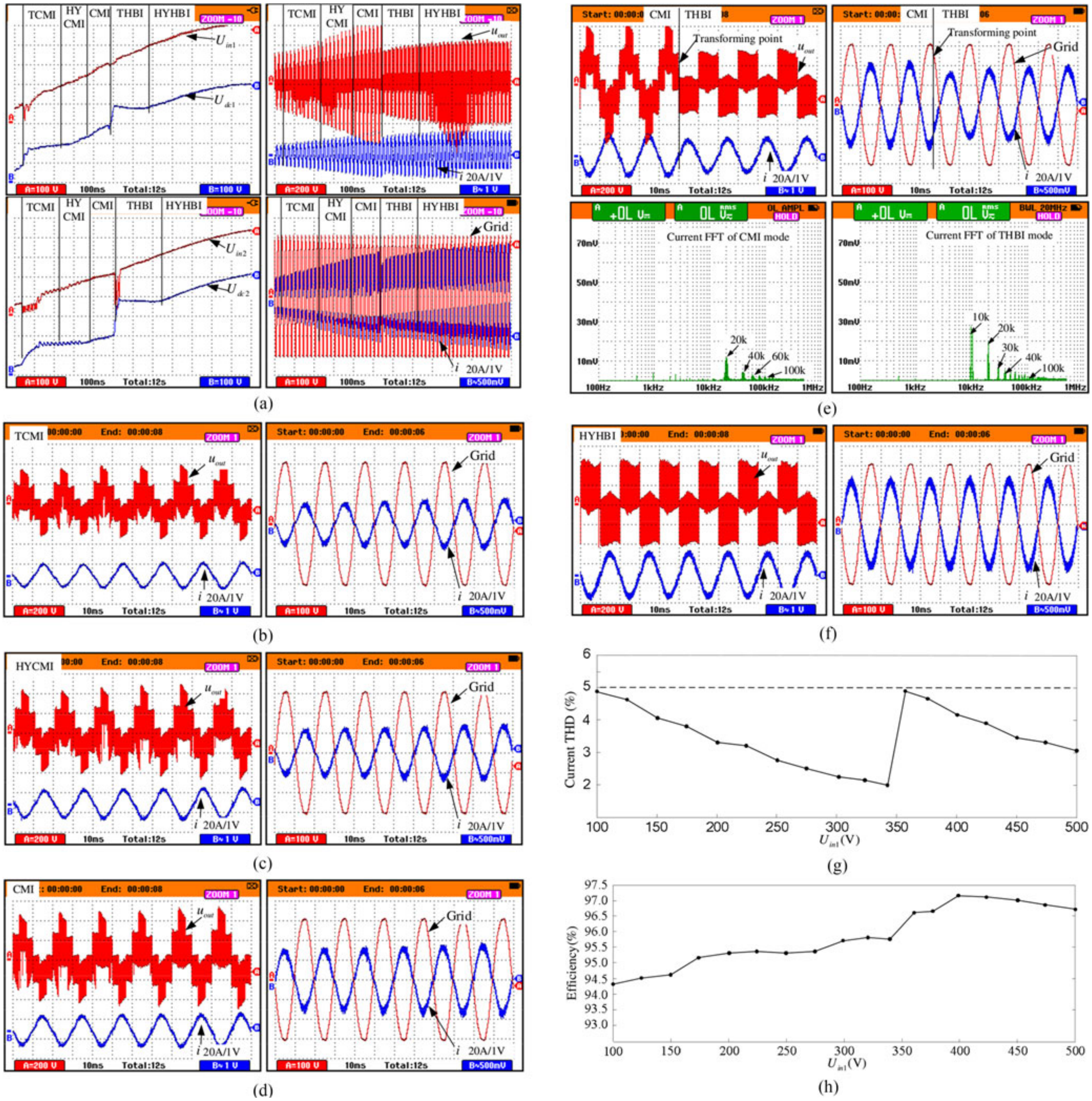

(a) (b) (c) (d) (e) (f) (g) (h)

Fig. 9. Experimental waveforms of proposed MTM-GCI. (a) Overall process; (b) TCMI mode; (c) HYCMI mode; (d) CMI mode; (e) around the point of transforming CMI into THBI; (f) HYHBI mode; (g) grid current THD; and (h) efficiency.

operational process, both the output voltages of the two RESs are consistent with their respective reference values and the relationship of $U_{\text{in1}} \approx \sqrt{3}U_{\text{in2}}$ is always maintained. It illustrates that the independent output power control of the two RESs is achieved.

Throughout the entire operational process, all of the topology modes have achieved the grid-connected operation. It can be known that the grid current remains sinusoidal and almost out of phase with the grid voltage. It means that the system works at nearly unity power factor. The actual grid current THDs corresponding to various output voltages of the RESs are tested and the curves are drawn in Fig. 9(g). The grid current THDs are always less than 5% in the entire operational range. It means that the proposed MTM-GCI possesses a wide operational range. The actual efficiency data are tested and the efficiency curve is drawn in Fig. 9(h). It can be seen that the efficiency of the inverter increases gradually by online transforming the complicated topology modes into the simpler ones and the maximum efficiency is 97.4%. The European efficiency of the proposed inverter is further calculated according to its definition. It is found to be 96.3%.

In order to more clearly demonstrate the superiority of the comprehensive performance of the proposed MCM-GCI, the MCM-GCI is compared with the dc optimizer and TCMI, as

TABLE II
DATA OF POWER SWITCHES USED IN THREE KINDS OF GCIS

Item	DC Optimizer	TCMI, Proposed
Operational range (V)	50–400	50–400
Max. dc-bus voltage (V)	800	400
Model number of IGBT	FF200R12KE4	FF200R06KE3
Rated voltage (V)	1200	600
Rated current (A)	200	200
Switching loss energy (mJ)	57	14.9
Rated conduction loss (W)	400	320
Cost ratio	2.3	1

TABLE III
DATA OF THREE KINDS OF GRID-CONNECTED INVERTERS

Item	DC optimizer	TCMI	Proposed
Number of power switch + AC-side filter inductor	4 + 4	8 + 1	9 + 1
Cost ratio	1.15 + 4	1 + 1	1.1 + 1
Lowest voltage of RES (V)	50	50	50
Max. current THD (%)	5	5	5
Min. current THD (%)	1	1	2
Max. efficiency (%)	95.7	96.2	97.6
European efficiency (%)	94.6	95.1	96.3

shown in Fig. 1(a) and (c), respectively. The comparison includes the number of power switches, the cost, the generation range of the RES, the grid current THD and the operational efficiency. The comparison is performed under the conditions of the same operational range and rated power. It is assumed that the output voltage range of the RES is from 50 to 400 V. Based on this, the model number of the power switch and the filter inductance of the dc optimizer are determined. Because the two dc–dc converters in the dc optimizer are connected in series, the maximum output dc-bus voltage is up to 800 V. It makes that the rated voltage of the power switch should be selected as 1200 V. While the rated voltage of the power switches of the other two topologies can be selected as 600 V. Furthermore, according to the datasheets of the determined power switches, the loss data and cost ratios of the two kinds of power switches are obtained and listed in Table II. As seen from Table II, the conduction loss, the switching loss energy and the cost increase accordingly with the increase of the rated voltage of the power switch. The experimental platform of the dc optimizer is built up with the determined power switches and the experimental results are obtained.

The data of the three topologies, including the number of power switches and filter inductors, the overall cost, the operational range, the maximum and minimum grid current THDs, the operational efficiencies and European efficiency are listed in Table III. Among them, the ac-side filter inductance of the dc optimizer is designed to be four times of that of TCMI and that of the proposed MTM-GCI. It is because when the carrier frequencies of the three topologies are selected the same, the equivalent switching frequency of the dc optimizer is only ¼ of those of the other two topologies. To obtain the desirable grid current THD, the inductance value of the ac-side filter inductance of the dc optimizer is designed somewhat bigger than that of the other two topologies. In addition, because the number and the power rating of the dc–dc converters embedded in the three topologies are the same, the data of the dc–dc converters are not contained in Table III. It can be seen from Table III that although the total number of the power switches in the dc optimizer is the smallest, because it uses the power switches with a higher rated voltage and a larger ac-side filter inductance, the cost and loss of the dc optimizer are the highest. As for the proposed MTM-GCI, the cost increases only close to 10%. In the proposed MTM-GCI, by transforming the system online among the five topology modes within the entire operational range, the grid current THD is always smaller than the specific standard and the European efficiency of the system increases significantly. The utilization of the RES is accordingly increased. It means that the proposed MCM-GCI possesses the optimal comprehensive performance.

Finally, the issue of the leakage current of the proposed MTM-GCI is briefly discussed here. At present, there are many approaches to eliminate the leakage current in the GCIs. The first one is to develop a new modulation strategy to keep the voltage of the parasitic capacitor constant [23], [24]. The second one is to add an active filter into the system to reduce the leakage current [25]. The last one is to introduce some power components into the inverter to provide new current flowing route and the voltage of the parasitic capacitor will be kept constant [26]. The approaches 1 and 2 can be combined with the proposed inverter to eliminate the leakage current and the structure of the proposed inverter does not need to change. It will be our future research work.

VI. CONCLUSION

In this paper, a novel MTM-GCI with five equivalent topology modes suitable for the RES-GGS was proposed based on the characteristics of the RESs that their output voltage and power vary in a wide range. The optimal operational range of each topology mode was given according to their own performance in the entire operational range. The system-level control strategy was proposed as well to achieve both the independent output power control of the RESs and grid current closed-loop control in each topology mode. By online transforming the topology modes of the system smoothly, the following advantages were obtained: a wide generation range of the RESs, an independent output power control of each RES, and a higher European efficiency in the entire operational range. The improvement of the comprehensive performance of the GCI will benefit the increase of the utilization rate of the RES, and as a result, the unit generation cost of the RES-GGS will be reduced and the competitiveness of the RES-GGS will be enhanced.

REFERENCES

[1] R. G. Wandhare and V. Agarwal, “Novel integration of a PV-wind energy system with enhanced efficiency,” *IEEE Trans. Power Electron.*, vol. 30, no. 7, pp. 3638–3649, Jul. 2015.

[2] L. Nousiainen, J. Puukko, and A. Maki, “Photovoltaic generator as an input source for power electronic converters,” *IEEE Trans. Power Electron.*, vol. 28, no. 6, pp. 3028–3038, Jun. 2013.

[3] X. Yuan, J. Chai, and Y. Li, "A transformer-less high-power converter for large permanent magnet wind generator systems," *IEEE Trans. Sustain. Energy*, vol. 3, no. 3, pp. 318–329, Jul. 2012.

[4] S. Qin, S. T. Cady, A. D. Dominguez-Garcia, and R. Pilawa-Podgurski, "A distributed approach to maximum power point tracking for photovoltaic submodule differential power processing," *IEEE Trans. Power Electron.*, vol. 30, no. 4, pp. 2024–2040, Apr. 2015.

[5] M. N. Kabir, Y. Mishra, and G. Ledwich, "Coordinated control of grid-connected photovoltaic reactive power and battery energy storage systems to improve the voltage profile of a residential distribution feeder," *IEEE Trans. Ind. Inform.*, vol. 10, no. 2, pp. 967–977, May 2014.

[6] J. Storey, P. R. Wilson, and D. Bagnall, "The optimized-string dynamic photovoltaic array," *IEEE Trans. Power Electron.*, vol. 29, no. 4, pp. 1768–1776, Apr. 2014.

[7] IEEE Recommended Practices and Requirements for Harmonic Control in Electrical Power Systems, *IEEE Standard 519-1992*, 1992.

[8] D. Li and Z. Zhu, "A novel integrated power quality controller for microgrid," *IEEE Trans. Ind. Electron.*, vol. 62, no. 5, pp. 2848–2858, May 2015.

[9] S. Qin, S. T. Cady, A. D. Dominguez-Garcia, and R. Pilawa-Podgurski, "A distributed approach to maximum power point tracking for photovoltaic submodule differential power processing," *IEEE Trans. Power Electron.*, vol. 30, no. 3, pp. 2024–2040, Mar. 2015.

[10] N. Femia, G. Lisi, G. Petrone, G. Spagnuolo, and M. Vitelli, "Distributed maximum power point tracking of photovoltaic arrays: Novel approach and system analysis," *IEEE Trans. Ind. Electron.*, vol. 55, no. 7, pp. 2610–2621, Jul. 2008.

[11] G. R. Walker and P. C. Sernia, "Cascaded DC-DC converter connection of photovoltaic modules," *IEEE Trans. Power Electron.*, vol. 19, no. 4, pp. 1130–1139, Jul. 2004.

[12] L. Zhang, K. Sun, and H. Hu, "A system-level control strategy of photovoltaic grid-tied generation systems for European efficiency enhancement, " *IEEE Trans. Power Electron.*, vol. 29, no. 7, pp. 3445–3453, Jul. 2014.

[13] Y. Kim, Y. Ji, and J. Kim, "A new control strategy for improving weighted efficiency in photovoltaic AC module-type interleaved flyback inverters," *IEEE Trans. Power Electron.*, vol. 28, no. 6, pp. 2688–2699, Jun. 2013.

[14] E. Villanueva, P. Correa, J. Rodríguez, and M. Pacas, "Control of a single-phase cascaded H-bridge multilevel inverter for grid-connected photovoltaic systems," *IEEE Trans. Ind. Electron.*, vol. 56, no. 11, pp. 4399–4406, Nov. 2009.

[15] Y. H. Liao and C. M. Lai, "Newly-constructed simplified single-phase multistring multilevel inverter topology for distributed energy resources," *IEEE Trans. Power Electron.*, vol. 26, no. 9, pp. 2386–2392, Sep. 2011.

[16] L. Liu, H. Li, and Y. Xue. "Decoupled active and reactive power control for large-scale grid-connected photovoltaic systems using cascaded modular multilevel converters," *IEEE Trans. Power Electron.*, vol. 30, no. 1, pp. 176–187, Jan. 2015.

[17] L. Zarri, M. Mengoni, and A. Tani, "Minimization of the power losses in IGBT multiphase inverters with carrier-based pulse width modulation," *IEEE Trans. Ind. Electron.*, vol. 57, no. 11, pp. 3695–3706, Aug. 2010.

[18] Z. Gmyrek, A. Boglietti, and A. Cavagnino, "Iron loss prediction with PWM supply using low- and high-frequency measurements: analysis and results comparison," *IEEE Trans. Ind. Electron.*, vol. 55, no. 4, pp. 1722–1728, Sep. 2008.

[19] F. J. Wu, B. Sun, J. Duan, and K. Zhao, "Online variable topology-type photovoltaic grid-connected inverter," *IEEE Trans. Ind. Electron.*, vol. 62, no. 8, pp. 4814–4821, Aug. 2015.

[20] P. Palanivel and S. S. Dash, "Analysis of THD and output voltage performance for cascaded multilevel inverter using carrier pulse width modulation techniques," *IET Power Electron.*, vol. 4, no. 8, pp. 951–958, Sep. 2011.

[21] Y. Yang, K. Zhou, and M. Cheng, "Phase compensation resonant controller for PWM converters," *IEEE Trans. Ind. Inform.*, vol. 9, no. 2, pp. 957–964, Sep. 2013.

[22] F. J. Wu, D. Sun, L. Zhang, and J. Duan, "Influence of plugging DC offset estimation integrator in single-phase EPLL and alternative scheme to eliminate effect of input DC offset and harmonics," *IEEE Trans. Ind. Electron.*, vol. 62, no. 8, pp. 4823–4831, Aug. 2015.

[23] X. Q. Guo, D. Xu, and B. Wu, "Common-mode voltage mitigation for back-to-back current-source converter with optimal space-vector modulation," *IEEE Trans. Power Electron.*, vol. 31, no. 1, pp. 688–697, Jan. 2016.

[24] G. Abhishek, S. Rajasekar, and R. Gupta, "A new modulation technique to eliminate leakage current in transformerless PV inverter," in *Proc. Eng. Syst.*, Allahabad, India, Apr. 12–14, 2013, pp. 1–6.

[25] D. Barater, G. Buticchi, E Lorenzani, and C Concari, "Active common-mode Filter for ground leakage current reduction in grid-connected PV converters operating with arbitrary power factor," *IEEE Trans. Ind. Electron.*, vol. 61, no. 8, pp. 3940–3950, Aug. 2014.

[26] Y. Zhou and H. Li, "Analysis and suppression of leakage current in cascaded-multilevel-inverter-based PV systems," *IEEE Trans. Power Electron.*, vol. 29, no. 10, pp. 5265–5277, Oct. 2014.

Fengjiang Wu (M'15) received the B.S., M.S., and Ph.D. degrees in electrical engineering from Harbin Institute of Technology (HIT), Harbin, China, in 2002, 2004, and 2007, respectively.

Since 2007, he has been with the Department of Electrical Engineering, HIT, where he is currently an Associate Professor. Since 2016, he has been with the School of Electrical and Electronic Engineering, Nanyang Technological University, Singapore, Singapore, as a Senior Research Fellow. His current research interests include the area of renewable energy generation, microgrid, multilevel inverter technology, and electrical machines drive.

Xiaoguang Li received the B.S. degree in electrical engineering, in 2015, from Harbin Institute of Technology, Harbin, China, where he is currently working toward the Ph.D. degree in electrical engineering.

His current research interests include in the field of grid-connected inverters for renewable energy generation system and microgrid.

Fan Feng received the B.S. and M. S. degrees in electrical engineering from Harbin Institute of Technology, Harbin, China, in 2011 and 2015, respectively. He is currently working toward the Ph.D. degree from the School of Electrical and Electronic Engineering, Nanyang Technological University, Singapore, Singapore.

His current research interest includes the grid-connected inverter for renewable energy generation and microgrid.

Hoay Beng Gooi (SM'95) received the B.S. degree in electrical engineering from National Taiwan University, Taipei, Taiwan, in 1978, the M.S. degree in power engineering from the University of New Brunswick, Fredericton, NB, Canada, in 1980, and the Ph.D. degree in power engineering from the Ohio State University, Columbus, OH, USA, in 1983.

From 1983 to 1985, he was an Assistant Professor with the Department of Electrical Engineering, Lafayette College, Easton, PA, USA. From 1985 to 1991, he was a Senior Engineer with Empros (now Siemens), Minneapolis, MN, USA, where he was responsible for the design and testing coordination of domestic and international energy management system projects. In 1991, he joined the School of Electrical and Electronic Engineering, Nanyang Technological University, Singapore, as a Senior Lecturer, where he has been an Associate Professor since 1999 and the Deputy Head of Power Engineering Division from 2008 to 2014. His current research interests include microgrid energy management systems, electricity markets, spinning reserve, energy storage, and renewable energy sources.